

# Fiber Optic Sensors for Detection of Sodium Plating in Sodium-Ion Batteries

Jonas Hedman, Ronnie Mogensen, Reza Younesi, and Fredrik Björefors\*

Cite This: *ACS Appl. Energy Mater.* 2022, 5, 6219–6227

Read Online

ACCESS |

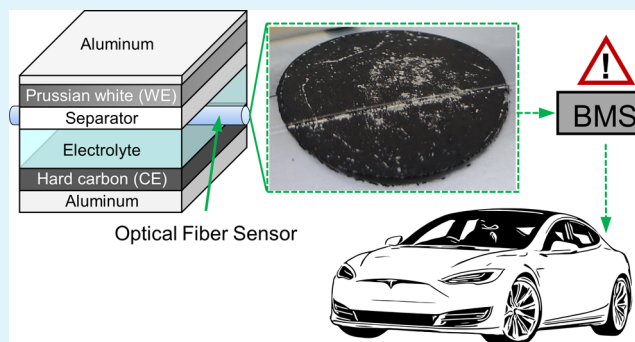
Metrics &amp; More

Article Recommendations

Supporting Information

**ABSTRACT:** Optical fiber sensors integrated into sodium-ion batteries could provide a battery management system (BMS) with information to identify early warning signs of plating, preventing catastrophic failure and maintaining safe operation during fast charging. This work shows the possibility of directly detecting plating of sodium metal in electrochemical cells by means of operando fiber optic evanescent wave (FOEW) spectroscopy. The results include measurements with FOEW sensors on bare copper substrates as well as on hard carbon anodes during operation in both half- and full-cell configurations. Full cells using hard carbon anodes and Prussian white cathodes with high areal capacities ( $>1.5 \text{ mAh cm}^{-2}$ ) and integrated FOEW sensors are shown to cycle well in pouch cells. The results also include measurements to demonstrate plating on hard carbon during sodiation at different rates.

**KEYWORDS:** evanescent waves, fiber optic sensors, hard carbon, Prussian white, sodium-ion batteries, sodium plating



## INTRODUCTION

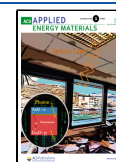
Sodium-ion batteries are gaining traction in the battery field as currently there are several attempts by different companies to commercially produce sodium-ion batteries. There are many reasons for this upswing, the biggest factors are without doubt the resource abundance, low-cost, and environmentally benign profile of most sodium-ion battery chemistries. Graphite does not intercalate any practical amount of sodium ions<sup>1</sup> unless specialized solvents that co-intercalate with the sodium ions are used.<sup>2</sup> This, in turn, has led to quite a lot of research initiatives to find alternative anode materials for sodium-ion batteries. Even though many alternatives such as tin, bismuth, and phosphorus have been tested with promising results, the standard material of choice is currently hard carbon.<sup>3</sup> Hard carbon, also known as non-graphitizable carbon, is often described as chaotically stacked graphite planes or as a “fallen house of cards” model.<sup>4</sup> This special structure enables hard carbon to intercalate sodium up to almost  $480 \text{ mAh g}^{-1}$  at potentials that are very close to the deposition of metallic sodium.<sup>5</sup> While these properties of hard carbon are most welcome, the low intercalation potential does create a risk for sodium plating during charge. Sodium metal is highly reactive and forms dendrites that can create short circuits, just like lithium dendrites in lithium-ion batteries. When comparing graphite and hard carbon it can be noted that the lower lithium staging plateau corresponding to  $\text{LiC}_6$  is ca. 70 mV from the equilibrium  $\text{Li}^+/\text{Li}$  potential<sup>6</sup> while hard carbon attains most of its capacity between 15 and 0 mV vs  $\text{Na}^+/\text{Na}$ .<sup>7</sup> This difference

is quite significant when it comes to safely operate sodium-ion batteries, especially during fast charging, and it is, therefore, essential to detect plating in cells to prevent accelerated degradation and remove the risk of short-circuiting by dendrites. Traditionally, plating is detected using slow cycling of sodium half cells or using three-electrode cells which allow a better observation of the anode potential.<sup>8</sup> As hard carbon goes from intercalation to plating of sodium on the surface, a small dip in potential is often seen, as a result of the overpotential required to nucleate sodium metal. After the first nucleation has occurred, the plating proceeds at a potential a few millivolts above the initial nucleation potential. In brief, this can be identified as when during discharge the  $dQ/dV$  becomes negative.<sup>4</sup> Other than that, plating has been studied by a wide range of experimental techniques such as nuclear magnetic resonance (NMR) spectroscopy,<sup>9,10</sup> neutron diffraction,<sup>11,12</sup> and operando microscopy,<sup>13</sup> and a more detailed description of available methods is given in a recent review article by Janakiraman et al.<sup>14</sup> Most of these alternatives are, on the other hand, often based on advanced and expensive lab-scale instrumentation of considerable size, more suitable for

Received: February 25, 2022

Accepted: April 11, 2022

Published: April 20, 2022



scientific experiments rather than detecting plating in real-life battery applications. Electrochemical methods based on differential voltage or capacity analysis in two-electrode cells are feasible for online monitoring but require very precise and accurate measurements, and the plating is indirectly detected from the discharge profile.<sup>14,15</sup>

In commercial batteries, three-electrode cells are not practical, and thus the producers are left to rely on pre-programmed cycling protocols and hope for the best if abnormal conditions in the cell initiate plating. By devising a fiber optic sensor that reliably detects plating before any significant amount of sodium has been deposited it would be possible to interrupt the charging or reduce the current to avoid cell failure.

In this work, we demonstrate that fiber optic evanescent wave (FOEW) sensors are able to detect the deposition of sodium metal on both copper foil and hard carbon electrodes. In the case of hard carbon, plating was detected both as a consequence of insufficient intercalation sites (i.e., poorly balanced cells or anodes with faded capacity) and as polarization-induced plating (i.e., excessive charging rates). The experiments have been carried out using commercially available electrodes in cell geometries that were unchanged except for the introduction of an optical fiber, 125  $\mu\text{m}$  in diameter, positioned between the hard carbon electrode and the separator. The work also demonstrates that the cycling performances of the full cells are not significantly affected when using the sensor and it shows the feasibility of detecting plating during fast charging of full cells.

## EXPERIMENTAL SECTION

**Optical Sensor Preparation and Sensor Integration.** FOEW sensors for integration into pouch cells were prepared by splicing two standard step-index multimode optical fibers (FG105LCA, Thorlabs), with a cladding diameter of 125  $\mu\text{m}$  and a core diameter of 105.5  $\mu\text{m}$ , to each end of a coreless optical fiber (FG125LA, Thorlabs) with a diameter of 125  $\mu\text{m}$ . Before splicing the optical fibers together, a portion of the polymer buffer/coating at each end of the multimode fibers was mechanically removed using a fiber stripper, and the ends were subsequently cut using a high-precision cleaver (FITEL S326A). The sensing region, which is a pure silica glass rod with a polymer coating, was prepared by removing the polymer by softening it with some acetone, then gently removing it with Kimtech wipes and cleaning it with some isopropanol. The coreless fiber was cut using the precision cleaver and spliced to multimode fibers using a FITELNINJA NJ001 fusion splicer (Furukawa Electric Co., LTD.) so that the final sensor length would equal 25 mm. The FOEW sensors were inserted into three-electrode pouch cells in transmission configuration and were pre-attached to the pouch material for easier handling and battery assembly inside the glovebox. The FOEW sensor was positioned at the surface of the working electrode in the half cells and at the counter electrode in full cells, and extra heat-sealing film was added around the edges of the pouch cells to ensure a hermetic sealing around the optical fiber entry and exit points.

**Cell Preparation.** All electrochemical experiments were carried out in three-electrode pouch cells with integrated FOEW sensors in either half- or full-cell configuration. Half cells for sodium plating experiments on both copper and hard carbon electrodes were assembled with sodium metal as the reference electrode. The copper electrodes were punched from high-quality copper foil into 20 mm disks and cleaned by ultrasonication in isopropanol for 30 min. Hard carbon electrodes used in both half- and full-cell experiments were prepared from commercial hard carbon (Kuraranode type 2) mixed with CMC and SBR and coated by LiFeSiZE AB with an active material mass loading of ca 7.84  $\text{mg cm}^{-2}$ . Full cells using Prussian white as cathodes and reference electrodes were assembled with hard

carbon as the working electrode. The Prussian white cathodes were prepared by LiFeSiZE AB and had an areal capacity of approximately 1.87  $\text{mAh cm}^{-2}$ . The reference electrodes were prepared from a Prussian white cathode that had been electrochemically desodiated to 3.3 V vs  $\text{Na}^+/\text{Na}$ . Metallic sodium counter electrodes were prepared by hydraulic pressing of sodium (Aldrich 99.9%) into a thin layer of sodium onto aluminum foil from which 20 mm disks were punched out before use. All handling of metallic sodium was carried out in an argon glovebox. The electrolyte used in all half and full cells was prepared inside an argon-filled glovebox by mixing ethylene carbonate (EC, BASF) and diethyl carbonate (DEC, Novolyte Technologies) in equal proportions by volume. Sodium hexafluorophosphate ( $\text{NaPF}_6$ , Stella), which was dried at 120  $^\circ\text{C}$  for 24 h under vacuum was subsequently dissolved in the solvent mixture to obtain a 1 M concentration. Glass-fiber separators (Whatman, GF/A) were punched to 30 mm disks which were dried for 12 h at 120  $^\circ\text{C}$  under vacuum and placed on top of the working electrode with the FOEW sensor. All cells were assembled using 300  $\mu\text{L}$  of the electrolyte added to the separator and vacuum-sealed under argon.

**Electrochemical Characterization.** All electrochemical tests were performed in a cleanroom environment with a controlled room temperature of  $21 \pm 1$   $^\circ\text{C}$  and was carried out on a Biologic VMP2 multichannel potentiostat/galvanostat. Galvanostatic cycling was performed on the half cells where three formation cycles at 0.1C were performed on the hard carbon electrode before slowly sodiating at a current corresponding to C/20. The C-rate was calculated based on the active material mass loading and a practical capacity of 300  $\text{mAh g}^{-1}$ . Formation cycling was performed between 0.005 and 1.6 V and for the slow sodiation at C/20, a time limitation of 40 h was used. In addition, sodium-hard carbon half cells were also discharged at 2C following cycling at 0.1C. Sodium plating was also carried out with copper foil as the working electrode using a constant current corresponding to what was used for the C/20 sodiation of the hard carbon half cells. The half-cell was kept at the open-circuit voltage for 5 min before the discharge current was applied, with a time limitation of 40 h. Galvanostatic cycling on three-electrode full cells was performed between 1.3 and 3.8 V. After four formation cycles at 0.1C, the charge rate was increased by stepwise increasing the charging current corresponding to 0.5, 1, and 2C, whereas the discharge current was kept constant at 0.1C. The C-rate was calculated based on the active material mass loading of the Prussian white cathode and a practical capacity of 150  $\text{mAh g}^{-1}$ . All cells were clamped with a layer of EPDM foam on each side of the pouch cell to get an even pressure distribution across the cells.

**Optical–Electrochemical Setup and Optical Measurement.** Pouch cells with an integrated FOEW sensor were connected to a commercially available optical unit (Insplorion AB) equipped with a stabilized tungsten-halogen light source and a UV–vis–NIR spectrometer for acquiring the optical signals. Multimode patch cables with standard FC/PC to SMA905 connections were used to connect the fiber optic sensor to the spectrometer and the broadband light source, and the three-electrode pouch cell was connected to the potentiostat/galvanostat. While cycling the battery cells, white light was coupled to the optical fiber from the broadband light source and the optical signal was collected with a charge-coupled device (CCD) detector. The sampling period of the spectrometer was set to 10 s for all experiments, and spectra were recorded between 500 and 900 nm. The spectra were averaged over 200 spectral acquisitions and the dark noise contribution was subtracted from the transmission intensities before normalization. The collected intensities were subtractively normalized according to  $\Delta I/I_0 = (I - I_0)/I_0$ , where  $I$  is the intensity measured continuously throughout cycling at each specific wavelength and  $I_0$  is the intensity at each specific wavelength at the beginning of sodiation. A Savitsky–Golay filter was used for post-processing of the optical signals to further reduce noise and increase precision without distorting the optical signal.

## RESULTS AND DISCUSSION

The evidence for the detection of sodium plating is most plainly given by demonstration in a very simple system (Figure 1a) constructed as follows: An optical fiber placed in contact

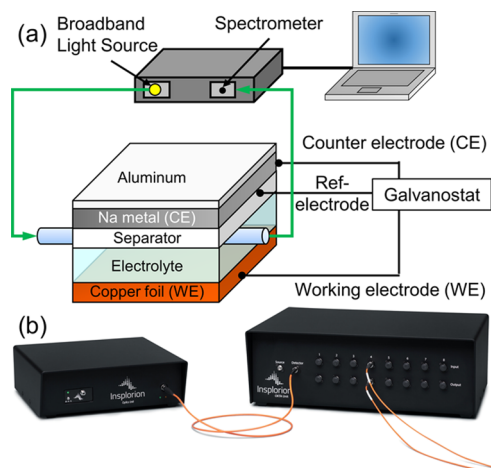


**Figure 1.** Schematic view of the optical–electrochemical setup with the FOEW sensor placed on the surface of a copper electrode in a copper–sodium half cell is shown in (a). Image of the optical unit is shown in (b).

with a copper foil acting as the working electrode in a pouch cell, and a glass-fiber separator which in turn is in contact with the sodium-metal counter and reference electrodes. The sensing region of the optical fiber (which has been described

in more detail elsewhere)<sup>16</sup> is consequently in direct contact with the working electrode, the glass-fiber separator, and the electrolyte. The integrated FOEW sensors were connected to an optical unit (Figure 1b) equipped with a stabilized broadband light source and a UV–vis–NIR spectrometer in transmission configuration, and the optical unit was controlled by a computer while cycling the batteries. White light was coupled to the optical fiber and the intensity output, modulated by the battery cell chemistry, was collected by a charge-coupled device (CCD) detector at wavelengths ranging from 500 to 900 nm. The optical signal was subtractively normalized according to  $\Delta I/I_0 = (I - I_0)/I_0$ , where  $I$  is the intensity continuously monitored throughout the experiments at each wavelength and  $I_0$  is the intensity at each wavelength collected before sodiation.

Detection of sodium plating was demonstrated in a simple system using copper foil as the working electrode and sodium metal, both as the counter and reference electrodes (Figure 2). The voltage profiles during the constant current experiment are shown in Figure 2a, and at the onset of plating, the intensity drops sharply (Figure 2b). In more detail, close to the nucleation potential (at about 7 min, see Figure 2c,d), there is a sharp and abrupt decrease in the normalized intensity for all wavelengths, which evolves at different rates, with the intensity output from longer wavelengths decreasing more than those for shorter wavelengths. The reduction of intensity shows an exponential decrease that continues until a steady state is reached and a saturated region emerges approximately 15 h into the experiment, after which all wavelengths show a more or less constant optical response as plating continues (Figure 2b). From Figure 2d, it is also clear that the optical response

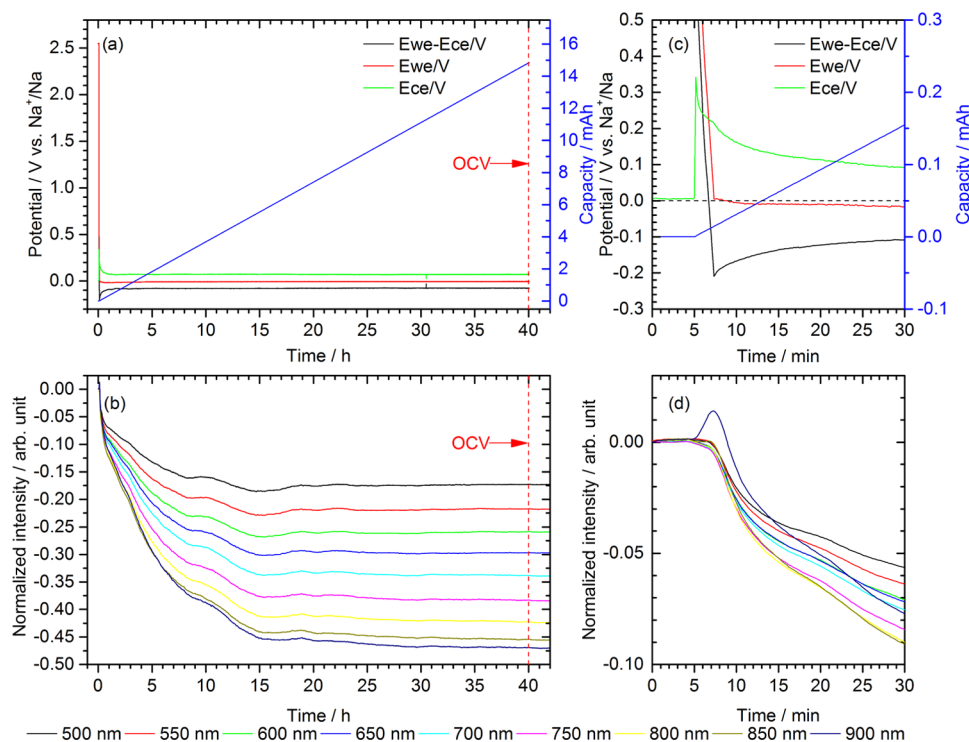


**Figure 2.** Voltage profiles of plating on a copper (WE) vs Na (CE) half cell with Na as the reference electrode using a constant current of approximately  $-0.118 \text{ mA cm}^{-2}$  shown in (a). Normalized intensity from the fiber optic sensor positioned between the copper electrode and the glass-fiber separator, monitored operando is shown in (b). A more detailed figure of the sodium nucleation and the corresponding intensity output is provided in (c) and (d), respectively. The red dashed line in (a) and (b) indicate when the plating experiment was finished and the cell is at the open-circuit potential.

from the cell remains unchanged during the pause before the current is applied. However, as the current of about  $-0.118 \text{ mA cm}^{-2}$  is applied to reduce sodium ions, there is an isolated response from the wavelengths between 850 and 900 nm, which gradually increases in intensity with wavelength until the potential of sodium deposition is reached (see Figure S1). The onset of plating based on the potential of the working electrode coincides with the maximum of the intensity for longer wavelengths and is also the point where the intensity at all wavelengths begins to show a clear decrease. It is important to note that the increase in intensity for wavelengths between 850 and 900 nm occurs prior to plating is detectable by observing the potential of the working electrode.

From Figure 3, the deposited sodium metal on the copper electrode shows a gray and mossy appearance and metallic

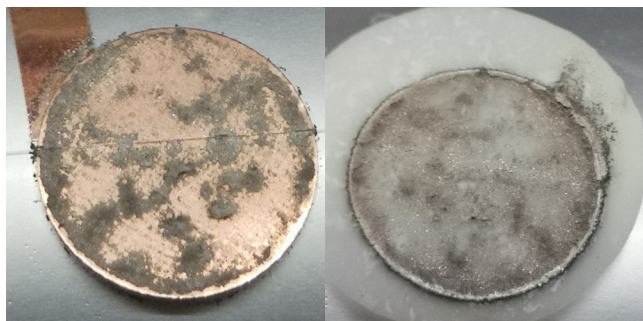


**Figure 3.** Copper working electrode after the plating experiment showing the fiber optic sensor, mossy metallic sodium, and traces of attached glass-fiber separator (left). Glass-fiber separator with the surface that was facing the copper working electrode showing that metallic sodium infiltrated the separator (right).

sodium is clearly visible around the edge of the separator, which is missing from the corresponding area on the copper working electrode. The post-mortem investigation of the cell also shows that the optical fiber is intact and that sodium metal has grown into the glass-fiber separator causing the separator to adhere to the copper electrode. It is also evident that sodium metal has been deposited on the entirety of the electrode, although the plating is not homogeneous.

The results from the plating experiment were also replicated in a similar system where the copper working electrode was substituted with a hard carbon electrode having an active material mass loading of  $\sim 7.84 \text{ mg cm}^{-2}$ . In this case, hard carbon was sodiated slowly at a rate of  $C/20$  and as the maximum capacity of  $300 \text{ mAh g}^{-1}$  was reached the potential of the working electrode clearly displays a nucleation dip (dashed line in Figure 4a,c). This nucleation dip (observed with the sodium-metal reference electrode) correlates perfectly with a decrease in the transmitted light intensity that is strikingly similar to the previously mentioned copper–sodium half cell (Figure 4b,d). The decrease in intensity continues as plating progresses, and the rate of intensity change remains wavelength dependent for at least 20 h, with longer wavelengths decreasing more than shorter wavelengths. At approximately  $580 \text{ mAh g}^{-1}$ , the decrease in intensity of all wavelengths with continued plating begins to subside, resembling the onset of the saturated region observed while plating on copper, which emerged after 15–20 h (see Figure 2). The plating on hard carbon, which begins at about  $300 \text{ mAh g}^{-1}$  and continues until the experiment is completed at  $600 \text{ mAh g}^{-1}$ , corresponds to ca 20 h and is comparable with the exponentially decreasing region in Figure 2. A noteworthy difference was also that instead of only 850–900 nm wavelengths showing a small increase in intensity before the

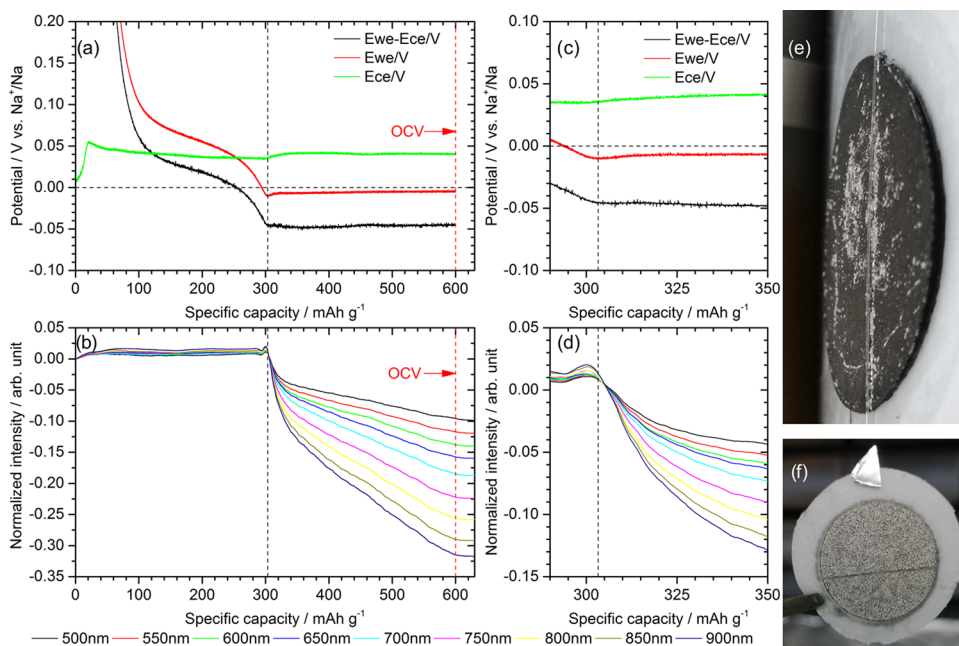


**Figure 4.** Sodiation of hard carbon at  $C/20$  (ca.  $-0.118 \text{ mA cm}^{-2}$ ) in a hard carbon (WE) vs Na (CE) half cell with Na as the reference electrode is presented in (a). The three-electrode pouch cell is fitted with a fiber optic sensor positioned at the surface of the hard carbon electrode and the corresponding intensity output monitored operando is shown in (b). The red dashed line in (a) and (b) indicates when the experiment was finished and the cell is at an open-circuit potential. A more detailed view of the sodium nucleation dip is provided in (c) and the corresponding intensity output is shown in (d). Post-mortem image of the hard carbon electrode shows the FOEW sensor and metallic sodium plated at the surface in (e) and the separator surface that was facing the hard carbon electrode, containing specks of metallic sodium is presented in (f).

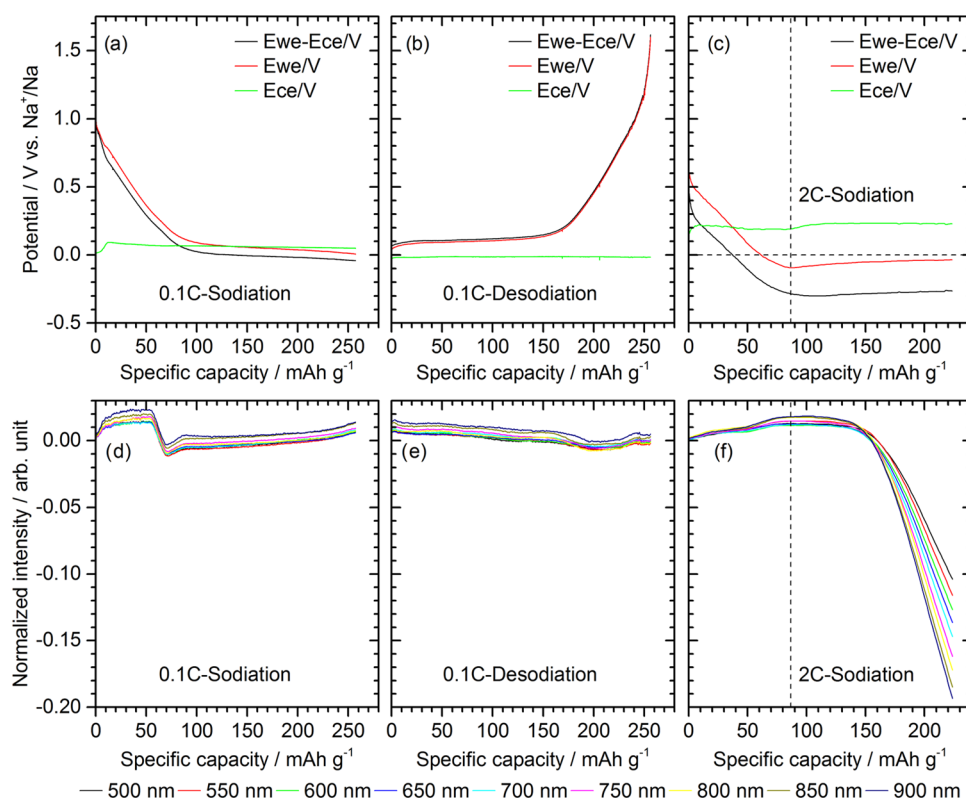


**Figure 5.** Fourth sodiation and desodiation of hard carbon at 0.1C (ca.  $-0.218 \text{ mA cm}^{-2}$ ) in a hard carbon (WE) vs Na (CE) half cell with Na as the reference electrode, with voltage profiles shown in (a) and (b) and the corresponding optical signals in (d) and (e), respectively. The voltage profile in (c) and optical signal in (f) show a 2C sodiation in the fifth cycle and the dashed line indicates the point where  $dQ/dV$  of the working electrode switches from positive to negative.

onset of plating, this increase is now evident for all wavelengths, although it remains the strongest for the longer wavelengths (Figure 4d).

Post-mortem studies of the hard carbon half cell show that the hard carbon working electrode has spotty sodium-metal deposits, both next to the fiber sensor and also in other regions across the electrode (Figure 4e). Post-mortem studies also revealed that significant plating occurred beneath the hard carbon, between the aluminum substrate and the hard carbon working electrode (Figure S2). Further examination of the separator also shows that sodium was homogeneously deposited and caught in the separator except for a thin trace where the fiber was located (Figure 4f).

Commercial full cells are quite sensitive to the active mass balance and geometric overlap between the anode and cathode. Any imbalance can lead to sodium plating, and since the introduction of an optical fiber constitutes a local electrode blockage, it is expected that it may have some impact on cycling performance. On the other hand, it has been demonstrated that optical fiber Bragg grating (FBG) sensors with the same glass-fiber dimensions, embedded in large-format lithium-ion batteries do not have a significant effect on performance in terms of cycle life and capacity retention, and after 140 cycles in such a cell, capacity fading was comparable with a reference LIB cell without the FBG sensor.<sup>17</sup> The shadow effect of the electrode would correspond to about 0.8 percent of the total area and could be considered negligible in terms of capacity but the effect is most likely larger for high-rate cycling.

To evaluate the FOEW sensor for fast charging applications, a second set of sodium-hard carbon half cells were assembled.

The aim for these cells was to rule out the possibility of plating due to insufficient capacity and test only for polarization-induced plating. This experiment was carried out by performing four slow (0.1C) formation cycles with the lower potential limitation set to 5 mV vs the sodium reference electrode, followed by a 2C sodiation that was capacity limited and terminated when 80% of the available sodium storage space based on the second formation cycle was reached (ca.  $223 \text{ mAh g}^{-1}$ ). After the 2C sodiation was completed, the cells were disassembled and post-mortem photographs were obtained (see Figure S3). Figure 5 shows the electrochemical and corresponding optical signals of the hard carbon during the fourth formation discharge and charge at 0.1C and the subsequent sodiation at 2C. At rapid sodiation, the effect of polarization due to the high current at 2C is clearly visible from both the counter and the working electrode potentials (see Figure 5c). Consequently, the potential of the working electrode drops below zero after only about  $60 \text{ mAh g}^{-1}$  and a sodium nucleation dip is indicated with a dashed line. It is also apparent that there are significant differences in the optical signal between the formation cycle (Figure 5d,e) and the signal for rapid sodiation (Figure 5f), which bears a strong resemblance to the intentional plating experiments performed on copper and hard carbon at a slow rate, showing the same wavelength-dependent sharp decrease in intensity output. Subsequent post-mortem investigation (Figure S3) also confirms that sodium has been plated on the hard carbon despite the intentionally low-capacity utilization (ca.  $223 \text{ mAh g}^{-1}$ ). A more detailed image of the pre-nucleation increase in intensity and the following plating during rapid sodiation (Figure 5c,f) is presented in Figure S4. A noticeable change in

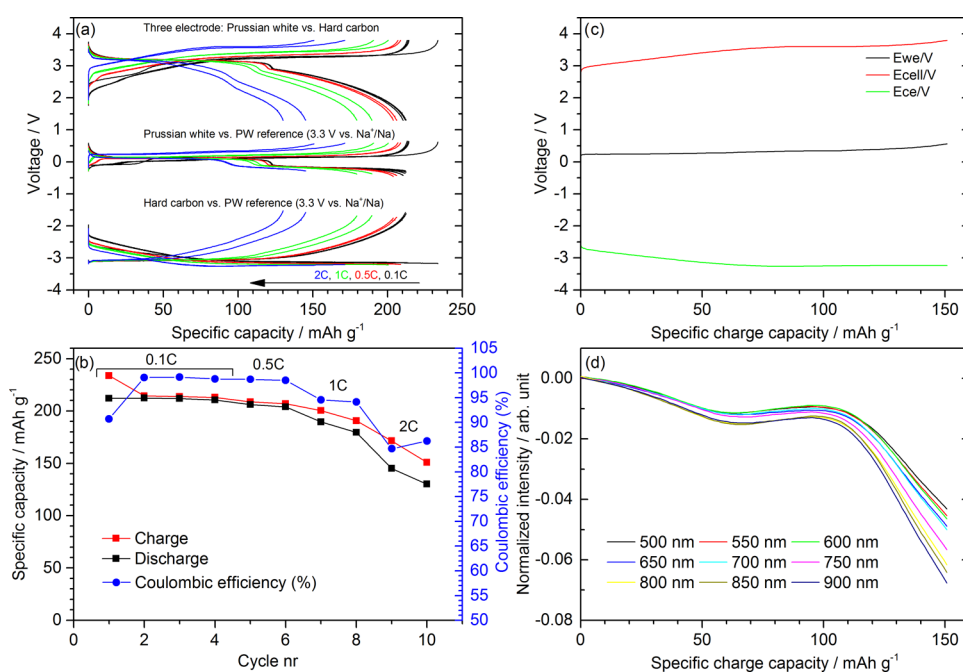


**Figure 6.** Prussian white (WE) vs hard carbon (CE) three-electrode full cell with desodiated Prussian white as the reference electrode. The voltages during constant current cycling at different rates are shown in (a) and the capacity and Coulombic efficiency are shown in (b). Voltage profiles for the last sodiation at 2C are presented in (c). The corresponding intensity output monitored in real-time at wavelengths ranging from 500 to 900 nm is shown in (d).

the rate of intensity increase can be seen close to  $50 \text{ mAh g}^{-1}$ , where the intensity at longer wavelengths (800–900 nm) begins to increase more than at shorter wavelengths, which is consistent with previous observations of the pre-nucleation increase in intensity. As plating initiates the intensity at all wavelengths begins to gradually decrease but initially at a slower rate compared to the previous plating experiments as a result of the simultaneous intercalation and plating. One should also note that while previous results were from slow cycling, the nucleation signal obtained in this case is from high-current short-duration experiments, and the high rate likely explains the rather drawn-out nucleation signal from both the electrochemical and optical signal response as there are still available intercalation sites. Consequently, the previously observed increase in intensity prior to plating, detectable by observing the working electrode potential, now persists over a longer time.

To further explore rate-induced plating, several full cells using hard carbon anodes, Prussian white cathodes, and reference electrodes with integrated FOEW sensors were assembled. The use of Prussian white reference electrodes enabled three-electrode cells where no metallic sodium is present and should thus replicate the cell chemistry of a commercial two-electrode cell. The areal capacity of the cathodes was ca  $1.87 \text{ mAh cm}^{-2}$ , which is close to what is common in batteries on the market today. The areal capacity of the anode was slightly overbalanced (ca. 28%) as is common in commercial cells to avoid plating. From an electrochemistry point of view, the performance of the cells is satisfactory and on par with cells that do not contain the optical fiber sensor (Figure 6a). The initial Coulombic efficiency reaches 90.72% during formation performed at 0.1C (Figure 6b), and this is close to market-leading performance in commercial sodium-ion cells.<sup>18</sup> The electrochemical stability with regards to capacity retention and Coulombic efficiency of the cells was

encouraging while the charging rate was kept low for the first four formation cycles, with the Coulombic efficiency reaching 98.78% within four cycles.

To evaluate the FOEW sensors' ability to detect plating in full cells, the cycling protocol was set to incrementally increase the charge rate after formation at 0.1C while maintaining the discharge rate constant at 0.1C. The incremental charging included two cycles at 0.5, 1, and 2C and was designed to subject the cell to currents beyond safe operating parameters and as also shown by previous experiments on half cells, plating was observed when the charge rate reached 2C. Again, the optical response from the 2C sodiation in full cells shows a similar wavelength-dependent sharp decrease in intensity beginning at around  $100 \text{ mAh g}^{-1}$  (see Figure 6d). The results from these measurements also show that although the optical response from the full-cell is similar to the half cell, the magnitude of the optical signal is a bit lower as compared to the slow half-cell cycling in Figure 4. This is not unexpected since the capacity obtained during plating in the half cell is larger compared to the full cell, which means more sodium has been deposited in the first case. Furthermore, there is no guarantee that sodium plating has not occurred to some extent in previous cycles, and this would lower the signal strength due to the normalization of intensity at the beginning of the cycle. It is, however, apparent that charging hard carbon at 2C again did produce metallic sodium at the anode, as evidenced by post-mortem studies (see Figure S5).

In standard optical fibers, light is guided in the core by total internal reflection at the interface between the core and the cladding of the lower refractive index as light is incident at an angle greater than the critical angle. When light propagates in the core, a standing wave is formed perpendicular to the core-cladding interface at each point of reflection and a part of the electromagnetic wave penetrates into the cladding.<sup>19–21</sup> This part is called an evanescent wave and its amplitude decays

exponentially with distance from the interface and falls off to almost zero within the cladding.<sup>22</sup> Therefore, in a standard optical fiber the evanescent field would decay long before it can reach the surrounding environment. By thinning out or completely removing the cladding, the optical fiber is made sensitive to the surrounding environment and can therefore be used as a sensor by allowing the evanescent waves to interact with the surrounding medium. If the medium is lossy, the evanescent wave can be absorbed and there is a net energy flow into the surrounding medium. As a result, the evanescent wave is weakened and the electromagnetic energy in the optical fiber becomes attenuated.<sup>19,23,24</sup>

In the sodium-ion battery cells, the electrolyte functions as a fiber cladding,<sup>25,26</sup> and the evanescent waves that form at the fiber core–electrolyte interface extend a short distance into the surrounding medium. As metallic sodium is deposited across the surface of the copper electrode or begins to plate on hard carbon, it is simultaneously deposited in the vicinity of the fiber optic sensor, strongly modulating the intensity output as the combination of sodium clusters and electrolyte forms a new lossy cladding. The sensitivity of the FOEW sensor is related to the degree of absorption of the surrounding medium, the number of reflections per unit length, and the penetration depth of the evanescent waves at the sensing region.<sup>27,28</sup> The latter is defined as the distance at which the electric field amplitude falls to  $1/e$  of its value at the core–cladding interface and depends on the wavelength of the incident light.<sup>19,20,22,23</sup> Longer wavelengths would thus translate into an increase in the penetration depth of the evanescent field, which is consistent with the stronger optical response at longer wavelengths during sodium plating on both copper and hard carbon electrodes.

Metals generally show high reflectance (above 80%)<sup>29</sup> in the visible spectral region which counterintuitively is due to their high absorption as the oscillations of free electrons in metals generate an electromagnetic wave which cancels the incoming wave in the metal, preventing the electromagnetic field from entering.<sup>30</sup> Consequently, the evanescent waves can only penetrate a short distance into the metal due to the very large absorption index of metals. However, one should also keep in mind that the deposited sodium metal is not exactly a smooth polished, and shiny metal surface, but rather shows a diffuse gray appearance based on the post-mortem studies and would also include a solid electrolyte interphase (SEI) layer at the surface. Any electromagnetic waves that are not absorbed by the metal are re-emitted, and the reflected light would depend on the scattering properties of the metal surface. As a result, the amount of light guided in the core of the optical fibers used in the pouch cells decreases as far as what the detector sees. It is also possible that some losses are introduced due to microbending of the fiber when metallic sodium forms near the fiber sensor, which would influence the guiding mechanism at the core–cladding interface. However, this does not explain the strong wavelength dependence since microbending in multimode optical fibers only contributes to a small wavelength-independent loss.<sup>31</sup> What could also be seen was that after a certain amount of sodium had been deposited on the electrode and around the sensing region, the signal became saturated and further plating did not influence the signal much as the surrounding environment most likely remained more or less the same within the sensing depth. A similar result has been observed when monitoring the rate of deposition of

polypyrrole<sup>32</sup> and metal thin films<sup>33</sup> on the uncladded sensing region of multimode optical fibers.

It was also observed that there is a pre-nucleation increase in intensity prior to the onset of plating on copper or hard carbon in half cells when plating occurs due to insufficient capacity. However, this pre-nucleation increase is not as apparent in the half-cell and full-cell experiments at a high rate (2C) when plating on hard carbon is induced by polarization and instead shows a more drawn-out appearance (Figures 5f and 6d) before the intensity is strongly attenuated. This behavior is reasonable since the available capacity is not fully utilized in the case of polarization-induced plating and sodium can still intercalate into hard carbon while simultaneously plating on the surface of the electrode. As a result, the intensity increase persists over a longer time span and thus changes the shape of the pre-nucleation peak compared to the half cells at a slow rate. This is, however, an important indicator as it appears before plating is detected electrochemically, and this will be the focus of future studies.

## CONCLUSIONS

This work shows that fiber optic sensors can be used for direct operando detection of sodium-metal plating in various cell configurations. There is a clear change in intensity at the onset of plating, and as the detection is performed directly at the surface of the anode it may provide additional details on the sodium intercalation and plating mechanism of hard carbon, information that will be difficult to obtain from the cell voltage alone as it is the difference of the average potential of the two electrodes. Furthermore, it is shown that the sensors can be mounted in regular pouch cells without interfering with cycling and that both plating at low and high rates can be detected. The information gained from the sensors can not only be used to detect plating but can yield information regarding the anode material, although hard carbon shows a weak optical signal change during sodiation and desodiation as compared to other anodes such as graphite. The mechanics of installing optical fibers in an industrial setting may not be trivial but if it could be done, it would provide some enticing benefits. A simple analysis method that can deliver direct feedback to the BMS to suspend dangerous charge operations could allow battery users to operate closer to the limits of their systems with reduced risks, providing safer and longer lasting batteries. The findings and experimental procedures of this work are also expected to be transferable for detecting plating in other battery systems, such as lithium plating on graphite or for characterization of anode-free batteries.

## ASSOCIATED CONTENT

### Supporting Information

The Supporting Information is available free of charge at <https://pubs.acs.org/doi/10.1021/acsaem.2c00595>.

Additional electrochemical and optical data on sodium plating on copper electrodes; post-mortem image of hard carbon; post-mortem images of hard carbon and the separator from rate-induced plating in half cells; electrochemical and optical data on rate-induced sodium plating on hard carbon; and post-mortem images of hard carbon and separator from plating experiments on full cells (PDF)

## AUTHOR INFORMATION

### Corresponding Author

Fredrik Björefors – Department of Chemistry—Ångström Laboratory, Uppsala University, SE-751 21 Uppsala, Sweden; [orcid.org/0000-0002-3598-3903](https://orcid.org/0000-0002-3598-3903); Email: [fredrik.bjorefors@kemi.uu.se](mailto:fredrik.bjorefors@kemi.uu.se)

### Authors

Jonas Hedman – Department of Chemistry—Ångström Laboratory, Uppsala University, SE-751 21 Uppsala, Sweden; [orcid.org/0000-0001-7246-1680](https://orcid.org/0000-0001-7246-1680)

Ronnie Mogensen – Department of Chemistry—Ångström Laboratory, Uppsala University, SE-751 21 Uppsala, Sweden

Reza Younesi – Department of Chemistry—Ångström Laboratory, Uppsala University, SE-751 21 Uppsala, Sweden; [orcid.org/0000-0003-2538-8104](https://orcid.org/0000-0003-2538-8104)

Complete contact information is available at: <https://pubs.acs.org/10.1021/acsaem.2c00595>

### Notes

The authors declare no competing financial interest.

## ACKNOWLEDGMENTS

StandUp for Energy, Skellefteå Kraft and Batteries Sweden (BASE)/Vinnova (project no. 2019-00064) are gratefully acknowledged for financial support. Insplorion AB is also acknowledged for support with optical equipment.

## REFERENCES

- (1) Ge, P.; Foulletier, M. Electrochemical Intercalation of Sodium in Graphite. *Solid State Ionics* **1988**, *28–30*, 1172–1175.
- (2) Jache, B.; Adelhelm, P. Use of Graphite as a Highly Reversible Electrode with Superior Cycle Life for Sodium-Ion Batteries by Making Use of Co-Intercalation Phenomena. *Angew. Chem., Int. Ed.* **2014**, *53*, 10169–10173.
- (3) Zhang, W.; Zhang, F.; Ming, F.; Alshareef, H. N. Sodium-Ion Battery Anodes: Status and Future Trends. *EnergyChem* **2019**, *1*, No. 100012.
- (4) Stevens, D. A.; Dahn, J. R. High Capacity Anode Materials for Rechargeable Sodium-Ion Batteries. *J. Electrochem. Soc.* **2000**, *147*, 1271–1273.
- (5) Kamiyama, A.; Kubota, K.; Igarashi, D.; Youn, Y.; Tateyama, Y.; Ando, H.; Gotoh, K.; Komaba, S. MgO-Template Synthesis of Extremely High Capacity Hard Carbon for Na-Ion Battery. *Angew. Chem., Int. Ed.* **2021**, *60*, S114–S120.
- (6) Reynier, Y.; Yazami, R.; Fultz, B. The Entropy and Enthalpy of Lithium Intercalation into Graphite. *J. Power Sources* **2003**, *119–121*, 850–855.
- (7) Kamiyama, A.; Kubota, K.; Nakano, T.; Fujimura, S.; Shiraishi, S.; Tsukada, H.; Komaba, S. High-Capacity Hard Carbon Synthesized from Macroporous Phenolic Resin for Sodium-Ion and Potassium-Ion Battery. *ACS Appl. Energy Mater.* **2020**, *3*, 135–140.
- (8) Li, Z.; Jian, Z.; Wang, X.; Rodríguez-Pérez, I. A.; Bommier, C.; Ji, X. Hard Carbon Anodes of Sodium-Ion Batteries: Undervalued Rate Capability. *Chem. Commun.* **2017**, *53*, 2610–2613.
- (9) Arai, J.; Okada, Y.; Sugiyama, T.; Izuka, M.; Gotoh, K.; Takeda, K. In Situ Solid State  $^7\text{Li}$  NMR Observations of Lithium Metal Deposition during Overcharge in Lithium Ion Batteries. *J. Electrochem. Soc.* **2015**, *162*, A952–A958.
- (10) Märker, K.; Xu, C.; Grey, C. P. Operando NMR of NMC811/Graphite Lithium-Ion Batteries: Structure, Dynamics, and Lithium Metal Deposition. *J. Am. Chem. Soc.* **2020**, *142*, 17447–17456.
- (11) Zinth, V.; von Lüders, C.; Hofmann, M.; Hattendorff, J.; Buchberger, I.; Erhard, S.; Rebelo-Kornmeier, J.; Jossen, A.; Gilles, R. Lithium Plating in Lithium-Ion Batteries at Sub-Ambient Temperatures Investigated by in Situ Neutron Diffraction. *J. Power Sources* **2014**, *271*, 152–159.
- (12) von Lüders, C.; Zinth, V.; Erhard, S. V.; Osswald, P. J.; Hofmann, M.; Gilles, R.; Jossen, A. Lithium Plating in Lithium-Ion Batteries Investigated by Voltage Relaxation and in Situ Neutron Diffraction. *J. Power Sources* **2017**, *342*, 17–23.
- (13) Chen, Y.; Chen, K.-H.; Sanchez, A. J.; Kazyak, E.; Goel, V.; Gorlin, Y.; Christensen, J.; Thornton, K.; Dasgupta, N. P. Operando Video Microscopy of Li Plating and Re-Intercalation on Graphite Anodes during Fast Charging. *J. Mater. Chem. A* **2021**, *9*, 23522–23536.
- (14) Janakiraman, U.; Garrick, T. R.; Fortier, M. E. Review—Lithium Plating Detection Methods in Li-Ion Batteries. *J. Electrochem. Soc.* **2020**, *167*, No. 160552.
- (15) Petzl, M.; Danzer, M. A. Nondestructive Detection, Characterization, and Quantification of Lithium Plating in Commercial Lithium-Ion Batteries. *J. Power Sources* **2014**, *254*, 80–87.
- (16) Hedman, J.; Nilebo, D.; Larsson Langhammer, E.; Björefors, F. Fibre Optic Sensor for Characterisation of Lithium-Ion Batteries. *ChemSusChem* **2020**, *13*, 5731–5739.
- (17) Raghavan, A.; Kiesel, P.; Sommer, L. W.; Schwartz, J.; Lochbaum, A.; Hegyi, A.; Schuh, A.; Arakaki, K.; Saha, B.; Ganguli, A.; Kim, K. H.; Kim, C.; Hah, H. J.; Kim, S.; Hwang, G.-O.; Chung, G.-C.; Choi, B.; Alamgir, M. Embedded Fiber-Optic Sensing for Accurate Internal Monitoring of Cell State in Advanced Battery Management Systems Part 1: Cell Embedding Method and Performance. *J. Power Sources* **2017**, *341*, 466–473.
- (18) Rudola, A.; Rennie, A. J. R.; Heap, R.; Meysami, S. S.; Lowbridge, A.; Mazzali, F.; Sayers, R.; Wright, C. J.; Barker, J. Commercialisation of High Energy Density Sodium-Ion Batteries: Faradion's Journey and Outlook. *J. Mater. Chem. A* **2021**, *9*, 8279–8302.
- (19) Hind, A. R.; Bhargava, S. K.; McKinnon, A. At the Solid/Liquid Interface: FTIR/ATR—the Tool of Choice. *Adv. Colloid Interface Sci.* **2001**, *93*, 91–114.
- (20) Mirabella, F. M. Internal Reflection Spectroscopy. *Appl. Spectrosc. Rev.* **1985**, *21*, 45–178.
- (21) Harrick, N. J. Electric Field Strengths at Totally Reflecting Interfaces. *J. Opt. Soc. Am.* **1965**, *55*, 851–857.
- (22) Leung, A.; Shankar, P. M.; Mutharasan, R. A Review of Fiber-Optic Biosensors. *Sens. Actuators, B* **2007**, *125*, 688–703.
- (23) Milosevic, M. Internal Reflection and ATR Spectroscopy. *Appl. Spectrosc. Rev.* **2004**, *39*, 365–384.
- (24) Wilks, P. A.; Hirschfeld, T. Internal Reflection Spectroscopy. *Appl. Spectrosc. Rev.* **1967**, *1*, 99–130.
- (25) Ghannoum, A.; Norris, R. C.; Iyer, K.; Zdravkova, L.; Yu, A.; Nieva, P. Optical Characterization of Commercial Lithiated Graphite Battery Electrodes and in Situ Fiber Optic Evanescent Wave Spectroscopy. *ACS Appl. Mater. Interfaces* **2016**, *8*, 18763–18769.
- (26) Hedman, J.; Björefors, F. Fiber Optic Monitoring of Composite Lithium Iron Phosphate Cathodes in Pouch Cell Batteries. *ACS Appl. Energy Mater.* **2022**, *5*, 870–881.
- (27) Ruddy, V.; MacCraith, B. D.; Murphy, J. A. Evanescent Wave Absorption Spectroscopy Using Multimode Fibers. *J. Appl. Phys.* **1990**, *67*, 6070–6074.
- (28) Khijwania, S. K.; Gupta, B. D. Fiber Optic Evanescent Field Absorption Sensor: Effect of Fiber Parameters and Geometry of the Probe. *Opt. Quantum Electron.* **1999**, *31*, 625–636.
- (29) Fox, M. *Optical Properties of Solids*, 2nd ed.; Oxford Master Series in Condensed Matter Physics; Oxford University Press: Oxford; New York, 2010; Vol. 3.
- (30) Milosevic, M. Metal Optics. In *Internal Reflection and ATR Spectroscopy*, Chemical Analysis: a Series of Monographs on Analytical Chemistry and Its Applications Ser; John Wiley & Sons: Hoboken, NJ, 2012; Vol. 262, pp 121–135.
- (31) Mitschke, F. Losses. In *Fiber Optics*; Springer: Berlin, Heidelberg, 2009; pp 75–84. DOI: 10.1007/978-3-642-03703-0\_5.
- (32) Jose, D.; John, M. S.; Radhakrishnan, P.; Nampoori, V. P. N.; Vallabhan, C. P. G. An Optical Fibre Based Evanescent Wave Sensor

to Monitor the Deposition Rate of Thin Films. *Thin Solid Films* **1998**, 325, 264–267.

(33) John, M. S.; Radhakrishnan, P.; Nampoore, V. P. N.; Vallabhan, C. P. G. A Fibre Optic Evanescent Wave Sensor for Monitoring the Rate of Pulsed Laser Deposition of Metal Thin Films. *Meas. Sci. Technol.* **1999**, 10, N17–N20.

## Recommended by ACS

### **Insight into the Contact Impedance between the Electrode and the Skin Surface for Electrophysical Recordings**

Liangtao Yang, Jinglong Wu, *et al.*

APRIL 14, 2022  
ACS OMEGA

[READ !\[\]\(0ac73c45806a78de248a19d9a2dbe7a6\_img.jpg\)](#)

### **Precise Analysis of Resistance Components and Estimation of Number of Particles in Li-Ion Battery Electrode Sheets Using LiCoO<sub>2</sub> Single-Particle Elect...**

Takahiro Saito, Shiro Seki, *et al.*

JULY 15, 2020  
THE JOURNAL OF PHYSICAL CHEMISTRY C

[READ !\[\]\(d3d0bc9cbc0b5499f7bfafd3278057f7\_img.jpg\)](#)

### **Electrochemical Surface Plasmon Resonance Spectroscopy for Investigation of the Initial Process of Lithium Metal Deposition**

Mitsunori Kitta, Hikaru Sano, *et al.*

JULY 14, 2021  
JOURNAL OF THE AMERICAN CHEMICAL SOCIETY

[READ !\[\]\(c3a92afbfbcda259fe6c9d5eed0857d1\_img.jpg\)](#)

### **Imaging Sensor for the Detection of the Flow Battery Via Weak Value Amplification**

Yang Xu, Yonghong He, *et al.*

SEPTEMBER 15, 2021  
ANALYTICAL CHEMISTRY

[READ !\[\]\(c44c1590e4070d8cc0b28ab85cb00ddf\_img.jpg\)](#)

[Get More Suggestions >](#)